Chinese Chemical Letters 36 (2025) 109687

Contents lists available at ScienceDirect

Chinese Chemical Letters

journal homepage: www.elsevier.com/locate/cclet

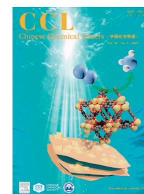

Epitaxial growth of full-vdW α-In_2Se_3/MoS_2 heterostructures for all-in-one sensing and memory-computing artificial visual system

Zheng Zhang[a,b,1], Lei Shi[a,b,1], Bin Wang[a,b,1], Jingyuan Qu[a,b], Xiaoling Wang[a,b], Tao Wang[a,b], Qitao Jiang[a,b], Wuhong Xue[a,b,*], Xiaohong Xu[a,b,*]

[a] *Key Laboratory of Magnetic Molecules and Magnetic Information Materials of Ministry of Education & School of Chemistry and Materials Science of Shanxi Normal University, Taiyuan 030031, China*

[b] *Collaborative Innovation Center for Advanced Permanent Magnetic Materials and Technology of Ministry of Education & Research Institute of Materials Science of Shanxi Normal University, Taiyuan 030031, China*

A R T I C L E I N F O

Article history:
Received 1 January 2024
Revised 10 February 2024
Accepted 29 February 2024
Available online 1 March 2024

Keywords:
Heterojunction
Ferroelectric
α-In_2Se_3/MoS_2
Band alignment
Optoelectronic
Artificial vision system

A B S T R A C T

Van der Waals (vdW) ferroelectric-semiconductor heterojunction provides reconfigurable band alignment based on optical/electrical-assisted polarization switching, which shows great potential to construct artificial visual neural systems. However, the mechanical exfoliation fabrication scheme for proof-of-concept demonstrations and fundamental studies is cumbersome and not scalable for practical application. Here, we present a synthetic strategy for the large-scale and high crystallinity growth of planar/vertical α-In_2Se_3/MoS_2 heterojunctions by dynamically tuning the growth temperature. Furthermore, based on the α-In_2Se_3/MoS_2 heterostructures, photo-synapse devices are designed and fabricated to simulate visual neural systems functions, including multistate storage, optical logic operation, potentiation and depression, paired-pulse facilitation (PPF), short-term memory (STM), long-term memory (LTM), and Learning-Forgetting-Relearning. By coupling the spatiotemporally relevant optical and electric information, the device can mimic the superior biological visual system's light adaptation and Pavlovian conditioning. This work provides a strategy for dynamically tuning the orientation of ferroelectric-semiconductor heterojunction stacks and will give impetus to applying all-in-one sensing and memory-computing artificial vision systems.

© 2025 Published by Elsevier B.V. on behalf of Chinese Chemical Society and Institute of Materia Medica, Chinese Academy of Medical Sciences.

To date, many efforts have been devoted to investigating vdW heterostructures with reconfigurable and high tunable band capability, which produce unique physical characteristics and enable totally new device functions [1–3]. However, Two-dimensional (2D) vdW heterostructures are confined mainly to mechanically exfoliated and restacked sheets, which are tedious and not scalable for practical techniques [4]. In addition, heterojunctions constructed by physical transfer are susceptible to polymer contamination and weak interfacial contact, which affects the optoelectronic properties of devices subject to interlayer coupling and interaction [2,5,6]. These obstacles have made them difficult to produce in a scalable way and have severely hampered applications in high-performance optoelectronic devices. In contrast, the chemical vapor deposition (CVD) technique circumvents the typical transfer steps and makes obtaining vertical or lateral heterojunctions easier with ultraclean interfaces and good contact [7–12].

Ferroelectric-semiconductor heterojunction provides reconfigurable band alignment based on optical/electrical-assisted polarization switching, which provides new degrees of freedom for device resistance manipulation in a noncontact and remote manner. It has been investigated and documented for applications such as photodetector [10,11,19], memory [13,14], artificial synapses [15-18,25,26], artificial visual neural systems [16-18,20-26], logical operation [22,27-29]. 2D ferroelectric materials, such as α-In_2Se_3, have attracted significant attention due to stable in-plane and out-of-plane interlocking ferroelectricity and tunable polarization state in monolayer thickness [19,28-33,35]. However, ferroelectric-semiconductor heterojunction based on the α-In_2Se_3 was rarely reported [16]. On the one hand, it is challenging to obtain large-scale α-In_2Se_3 flakes with few layers by the mechanical exfoliated strategy due to the strong coupling between the layers. On the other hand, regular 2D crystals are intolerant of thermally induced degradation and are too fragile to withstand the consecutive CVD steps required to form α-In_2Se_3 heterojunction. Therefore, it is crucial to investigate a method for fabricating ultrathin, high-quality, highly-crystalline,

* Corresponding authors.
E-mail addresses: xuewuhong@sxnu.edu.cn (W. Xue), xuxh@sxnu.edu.cn (X. Xu).
[1] These authors contributed equally to this work.

https://doi.org/10.1016/j.cclet.2024.109687
1001-8417/© 2025 Published by Elsevier B.V. on behalf of Chinese Chemical Society and Institute of Materia Medica, Chinese Academy of Medical Sciences.

large-size ferroelectric-semiconductor heterojunctions based on α-In_2Se_3.

Here, we report a synthetic approach for the large-scale and high crystallinity growth of planar/vertical α-In_2Se_3/MoS_2 heterojunctions by dynamically tuning the growth temperature. Vertically stacked heterojunctions can be obtained in the high-temperature zone of about 550–600 °C; Planarly stacked heterojunctions can be obtained by temperature exceeding 600 °C and the maximum size of 100.5 µm. Subsequently, Raman spectra and X-ray photoelectron spectroscopy (XPS) measurements are plotted to confirm the composition of heterojunctions. The High-resolution transmission electron microscopy (HRTEM) studies exhibit an atomically clean interface and excellent interfacial contact of the vertical heterostructure. More importantly, ferroelectric field effect transistors (FeFETs) based on vertical α-In_2Se_3/MoS_2 heterojunctions show a significant photoresponse in the visible wavelength range (from 359 nm to 671 nm), and α-In_2Se_3 exhibits light-induced changes in the polar ordering. By coupling optically assisted polarization switching and electrostatic gating effect, this device implements not only multistate storage and optical logic operation but also various biological visual neural network functions, including potentiation and depression, PPF, STM to LTM transition, Learning-Forgetting-Relearning, light adaptation, and Pavlovian conditioning. Overall, this work proposes an effective method for synthesizing planar/vertical α-In_2Se_3/MoS_2 heterojunctions and may open a new avenue for constructing all-in-one artificial visual neural networks.

Fig. 1a and Fig. S1 (Supporting information) schematically illustrate the synthesizing process of α-In_2Se_3/MoS_2 heterostructures through the two-step CVD epitaxial method. In the first step, monolayer MoS_2 films were obtained by epitaxy on SiO_2/Si with (110) orientation using the CVD technique, as described in the Methods section (Fig. S2 and S3 in Supporting information). In the second step, the MoS_2 obtained in the previous process was utilized as the heterojunction substrate (Figs. 1d and e). The Se (low-temperature region) and In_2O_3 (high-temperature region) powders were used as precursors, lateral epitaxy and vertical growth of the In_2Se_3/MoS_2 heterojunction to be controlled by growth temperature (Fig. S4 in Supporting information). Notably, 2D crystals that consist of only one or a few atomic layers are essentially intolerant to thermally induced degradation. In previous studies, mica was chosen as the universal substrate for α-In_2Se_3 epitaxy, and growth temperature was predominantly 700–800 °C [30,36-38]. High growth temperatures severely limit the application of α-In_2Se_3 films in large-scale integrated heterojunction devices. However, this study demonstrates that using MoS_2 as a substrate successfully reduces the growth temperature of α-In_2Se_3 to a range of 550–600 °C. Defects on the surface and edges of MoS_2 provide nucleation sites that significantly suppress the energy barriers for atomic nucleation, enabling robust large-scale growth of atomically thin 2D heterostructures.

Furthermore, we discovered that the growth temperature plays a crucial role in determining the direction of heterojunction stacking. Vertical heterojunctions are more likely to be formed at about 550 °C, whereas planar heterojunctions are more common above 600 °C (Figs. 1b and c). The atomic force microscope and optical images (Figs. 1f-i) demonstrate the morphology and thickness of horizontal/vertical heterojunctions, and it is evident that planar heterojunctions are more accessible to obtain atomic-level thickness. The mechanism of screening planar/vertical heterojunctions by controlling the growth temperature may result from the distinct thermodynamic stability of molecular clusters. According to the Burton-Cabrera-Frank theory of surface growth, the growth process is influenced by the diffusion capacity of the adsorbed cluster of atoms [34]. Adjusting the level of the diffusion barriers by temperature can determine the site of particle adsorption. During the epitaxial process, the molecular clusters in the atmosphere are adsorbed onto the surface of MoS_2. Variations in growth temperature affect the thermodynamic stability of the adsorbed atoms. Lower temperatures lead to more stable molecular clusters with higher diffusion barriers, resulting in vertical heterojunctions formed. Conversely, higher temperatures degrade the thermodynamic stability and the diffusion barriers, and due to the presence of unsaturated covalent bonds of sulfur atoms, the α-In_2Se_3 molecular are more stable when adsorbed at the edges of MoS_2, resulting in planar heterojunctions.

Next, we characterized the crystal quality and atomic structures of the α-In_2Se_3/MoS_2 vertical heterostructures. Fig. 2a presents the Raman mapping image of the heterostructure, confirming its composition. Raman spectra are plotted in Fig. S5a (Supporting information). Typically, the α-phase In_2Se_3 exhibits three characteristic peaks at 108, 175, and 206 cm^{-1}, corresponding to A_1(LO+TO) mode, A_1(TO) mode, and A_1(LO), which is in agreement with earlier work [30]. The XPS spectra show that the signatures of In and Se elements correspond to In and Se 3d states, which exhibit exceptional crystal quality without any alloying (Figs. S5b and c in Supporting information). The α-In_2Se_3/MoS_2 heterostructures show significant photoluminescence (PL) quenching with virtually undetectable PL, which may be caused by the energy transfer of α-

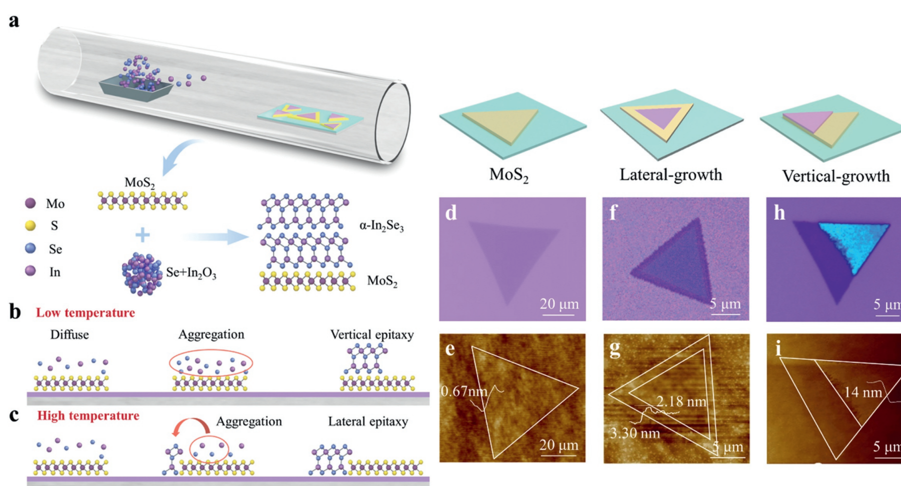

Fig. 1. Synthesis of 2D α-In_2Se_3/MoS_2 heterojunction. (a) Schematically illustrate the synthesizing process of α-In_2Se_3/MoS_2 heterostructures through the two-step CVD epitaxial method. (b, c) 2D nucleation process of the vertical and lateral heterostructures. Optical and atomic force microscope images of (d, e) MoS_2, (f, g) lateral α-In_2Se_3/MoS_2 and (h, i) vertical stacked α-In_2Se_3/MoS_2.

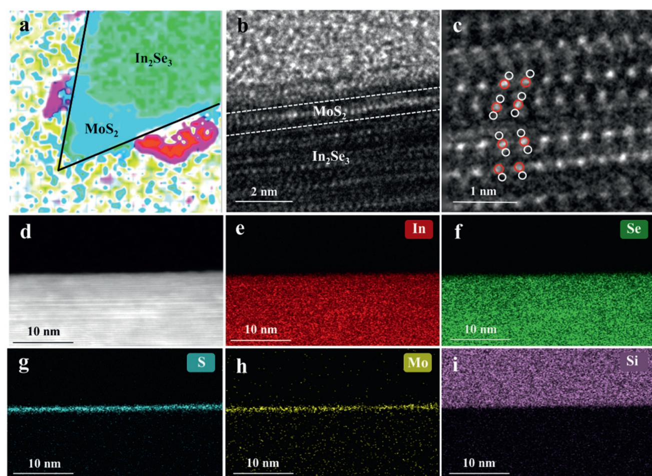

Fig. 2. Structure characterization of the vertically stacked α-In_2Se_3/MoS_2 heterostructures. (a) Raman mapping at 404.6 cm^{-1}. (b, c) Cross-sectional HRTEM image. (d-i) High angle annular dark field and EDS mapping images near the heterojunction interface.

In_2Se_3/MoS_2 interaction (Fig. S6 in Supporting information). Figs. 2b and c show enlarged HRTEM images of In_2Se_3 films, indicating that the adjacent "Se-In-Se-In-Se" atomic layers show an antiparallel arrangement, a typical feature of the 2H phase. The energy-dispersive X-ray spectroscopy (EDS) element maps revealed uniform distributions of Mo/S and In/Se while presenting a boundary between the two elements (Figs. 2d-i and Fig. S7 in Supporting information). The TEM studies exhibit an atomically clean interface and excellent interfacial contact of the vertical heterostructure.

To investigate the charge transport properties and optoelectronic performance of α-In_2Se_3/MoS_2 vertical heterostructures, FeFETs were designed and fabricated, with Cr/Au as the source-drain electrode and Si substrate as the back-gate electrode, and channel widths approaching 8.0 µm, depicted in Fig. 3a. The optical microscope image of the FeFETs is shown in Fig. S8 (Supporting information). The thickness of the α-In_2Se_3 and MoS_2 is 10.7 and 0.68 nm, respectively. Fig. 3b shows the intrinsic band alignment between few-layer α-In_2Se_3 and monolayer MoS_2 relative to the vacuum level, in combination with the Kelvin probe force microscope and PL results, which gave α-In_2Se_3 and MoS_2 band gap values of 1.53 and 1.83 eV, and work function values of 4.58 and 4.11 eV, respectively (Fig. S9 in Supporting information). Moreover, in previous studies, theoretical calculations have shown that the energy band arrangement of heterojunctions is not a simple superposition of the two films, which are influenced by the ferroelectric polarization field [39,40]. When the polarization is pointed downwards, the bands of the heterostructure form a type-I band arrangement. In contrast, the heterostructure has a type-II band arrangement when the polarization direction of α-In_2Se_3 is upward (Fig. S10 in Supporting information) [32,34,41,42]. The type-I alignment promotes photogenerated electron-hole recombination, and type-II alignment promotes efficient electron-hole separation. Control of the polarization direction manipulates the arrangement of the band structure, enabling ferroelectric-semiconductor heterojunctions to exhibit enormous potential for development in optoelectronic devices.

Fig. 3c presents the transfer properties, with the gate voltages (V_g) sweep of −30 V to 30 V, a device on/off ratio of up to 10^5 is possible, and the maximum memory window is 13.5 V. The FeFETs showed typical n-type semiconductor behavior with anticlockwise hysteresis, which can be attributed to the ferroelectric polarization switching of the α-In_2Se_3; the device exhibited distinct resistance states depending on the polarization direction. Fig. S11 (Supporting information) shows the output characteristics at different gate voltages, with saturation current increasing rapidly with V_g. The linearity of current-voltage in the variable resistance region suggests that the source-drain electrode exhibits ohmic contact with α-In_2Se_3 and MoS_2 films. Fig. S12a (Supporting information) demonstrates that applying $a \pm 50$ V, 30 s pulse results in the downward/upward polarization state, and the device turns to the low/high-resistive state. The device exhibits an on/off ratio exceeding 10^3, and negligible degradation even after 10^4 s (Fig. S12b in Supporting information). The low/high-resistive state can be clearly distinguished up to an extrapolation of 1 year, as depicted by the dashed gray lines in Fig. S13 (Supporting information). The high-quality α-In_2Se_3/MoS_2 interface suppresses leakage current and ion diffusion, which is responsible for this excellent retention and endurance.

Photoresponse properties of the device were further discussed with different wavelengths of laser, respectively. Prior to each photoelectronic performance measurement, an electrical pulse of −50 V was applied for 30 s to switch the polarization to the downward state. This initialization process ensures that all photoelectronic measurements are performed under the same polarization conditions. The laser is selectively focused on the channel of the device, avoiding a significant contribution of thermal gradients to the photoresponse. Fig. 3d shows the transfer curves under the illuminations of 359, 457, 532, 590, and 671 nm (5.75 mW/cm^2), respectively. The highest photocurrent extracted from the transfer curves is below 359 nm, indicating an efficient light absorption effect. In addition, we found that the photoelectric response of the devices with different polarization states (±50 V, 30 s) is significantly distinct, and the photocurrent ratio under positive/negative polarization states reaches two orders of magnitude (Fig. 3e). Furthermore, after excitation by ten consecutive light pulses (5.75 mW/cm^2, 200 ms), the device exhibits a more robust, non-volatile ability in the downward polarization direction. The photocurrent can be maintained for hundreds of seconds after removing the light pulse. (Fig. 3f).

From the above results, it can be concluded that ferroelectric polarization plays a vital role in the modulation of the heterojunction band alignment. Fig. S14 (Supporting information) describes the mechanism of the optically assisted polarization switching and electrostatic coupling effect at the heterojunction interface. The α-In_2Se_3/MoS_2 heterojunction grown on a heavily doped p-type Si substrate is transferred to the Pt substrate by the PMMA-assisted method (see Experimental Section in Supporting information for details). First, we investigate the polarization-tunable properties of α-In_2Se_3. $A \pm 5$ V bias was applied to scan box-in-box patterns, presenting a solid phase contrast of ≈ 180° of out-of-plane direction and the corresponding standard butterfly amplitude loop with a 180° flip (Figs. S15 and S16 in Supporting information). Piezoelectric force microscope images showed a predominantly downward polarization state of initial α-In_2Se_3, which is probably due to the vacancies/defects present on the surface, resulting in the built-in field (E_{bi}) at the In_2Se_3/MoS_2 interface (state I in Fig. S14). Thereby, the intrinsic heterojunction shows a type-I band structure. Then, a bias of −6.5 V was applied to switch the polarization state to the upward state while the band structure changed from type-I to type-II (state II in Fig. S14). The excellent contact of α-In_2Se_3/MoS_2 provides a platform for charge storage, where electron injection overcompensates for the polarization-bound charge, and additional electrons are stored at the interface, which results in field E^* reinforcing E_{bi} to stabilize the downward direction. Eventually, under ultraviolet (359 nm, 5.8 mW/cm^2) illumination for 30 min, the photon-generated carriers are separated by the electric field E^*, with the holes drifting to the α-In_2Se_3/MoS_2 interface to compensate for the injected electrons. The accumulation of holes causes a gradual reversal of E^*, resulting in E^* competing with E_{bi} and the

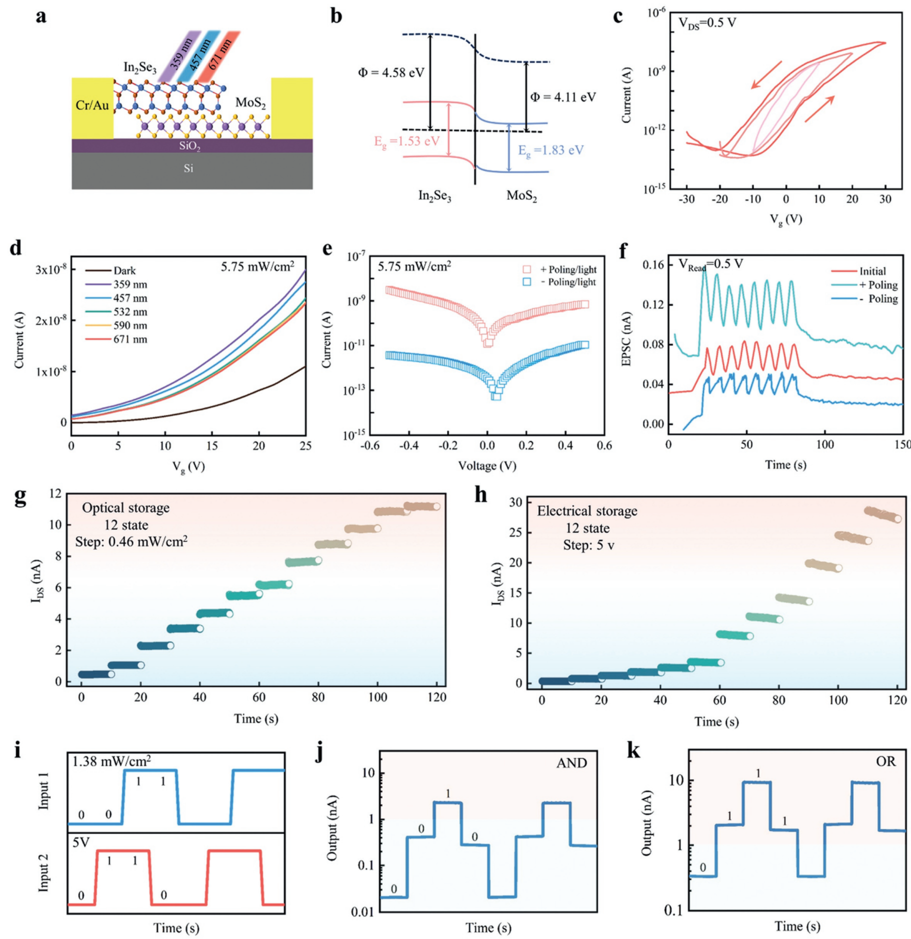

Fig. 3. Electrical and photoelectrical characterizations of the α-In_2Se_3/MoS_2 FeFET devices. (a) Schematic illustration of the vertically stacked α-In_2Se_3/MoS_2 vdW heterostructure-based device. (b) Schematic band structure of In_2Se_3/MoS_2. (c) Transfer curves of α-In_2Se_3/MoS_2 FeFETs. (d) Transfer characteristics in dark and under laser illumination. (e) *I–V* curves at positive polarization and negative polarization states under illumination. (f) The current curves of the three polarization states are a function of time under 359 nm multi-pulse illumination. (g) Optical-assisted multistate storage. (h) Electrostatic gating multistate storage. (i) Input signals for logic circuits. (j) Output signals for AND and OR logic circuits.

polarization direction turning downward. The band structure gradually transitions from type-II to type-I (state III in Fig. S14). Due to the excellent contact of the α-In_2Se_3/MoS_2 interface, the holes can be maintained for a longer period of time, and the upward polarization state remained stable after 24 h. (sate IV in Fig. S14). In conclusion, the polarization direction of the α-In_2Se_3/MoS_2 heterojunction is programmed by visible light to produce tunable band structures, based on which the reconfigurable photoelectric performance can be implemented.

Optically assisted multistate storage characteristic endowing the individual or synergistic sensing and elastic modulation of optical and electrical information, which was highly desirable for achieving the all-in-one sensing and memory-computing device [16,43]. Fig. 3g shows that 12 well-defined resistance states are obtained by precise modulation of the UV light intensity (about 0.46 mW/cm^2 per interval). As laser power density increases, the distinction between resistive states becomes blurred, indicating that the photocurrent approaches saturation. Limited by experimental conditions (laser power density step), more resistance states can be achieved otherwise. Similarly, we achieved electrostatic gating multistate storage by applying a series of polarization pulses (5 V per interval) above the coercive voltage to the FeFET devices and obtaining 12 resistive states (Fig. 3h). Opposite to the light-controlled storage effect, static gate voltage can control carrier concentration, resulting in a more pronounced difference between adjacent resistive states. The above results confirm that the device's optical/electrical sensing and storing properties establish two degrees of freedom to define the optoelectronic performance of the α-In_2Se_3/MoS_2 heterojunction.

To illustrate the application of reconfigurable FeFET devices to digital logic circuits, we present AND and OR logic gate operations on a single device. Here, laser intensity and V_g were used as two-input signals in the logic gates, which are denoted as 'Input 1' and 'Input 2'. The logic functions of AND and OR are modulated depending on the drain-source voltage, which is 1.0 V for AND and 1.5 V for OR. Both logic operations were performed with the same input signal (1.38 mW/cm^2, 10 V) (Fig. 3i). We define the output current of more than 1 nA as the logic state '1'; otherwise, the output current has been assigned to '0'. For the AND gate operation, the high state, '1', was only at (Input 1, Input 2) = (1, 1) (Fig. 3j). However, for the OR gate operation, the low state, '0', was only at (Input 1, Input 2) = (0, 0) (Fig. 3k).

As mentioned above, the photoelectrical characteristics of the FeFET devices are reconfigurable by changing the polarity of α-In_2Se_3 and the intensity of visible light. By exquisitely tuning the device resistance through ferroelectric polarization and electrostatic gating, we achieve photoelectric response, multistate storage and logic operations for programmable all-in-one sensing and memory-computing applications.

Artificial visual neural networks with temporal windows of synaptic plasticity can be realized by combining the tunable laser parameters and V_g with the ferroelectric and optoelectronic prop-

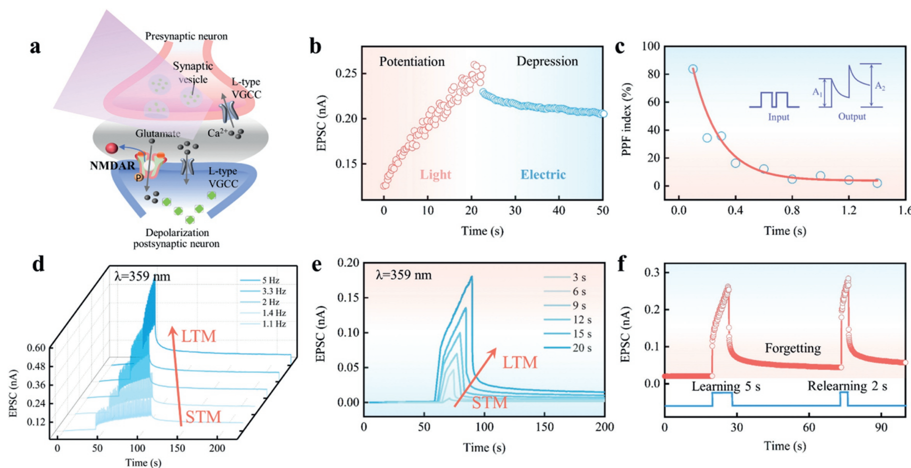

Fig. 4. Simulation of various functions of photo-synapses. (a) Schematic diagram of the biological photo-synapse. (b) Light-induced potentiation and electrical-induced depression effect. (c) PPF ratio as a function of the pulse interval, defined as $(A_2 - A_1)/A_1 \times 100\%$, where the red line represents fitting results using the double exponential decay function. (d) Pulse frequency induces a transition from STM to LTM. (e) Pulse duration time induces a transition from STM to LTM. (f) Learning-Forgetting-Relearning behavior stimulated by two light pulses.

erties in the α-In_2Se_3/MoS_2 FeFETs [16-18,21]. Fig. 4a shows a schematic diagram of the biological photo-synapses, the basic unit of the retina and human visual system. Following light stimulation, the presynaptic neuron experiences an influx of Ca^{2+}, and neurotransmitters in synaptic vesicles are captured and released by the postsynaptic membrane. Then, the postsynaptic membrane generates an action potential, through which light information is perceived by the photo-synapses and transmitted to the visual neural network in the human brain. Fig. 4b shows the optical potentiation ($\lambda = 359$ nm) and electrical depression responses of the α-In_2Se_3/MoS_2 FeFETs; the light-induced polarization and electrostatic gating can trigger a well-linear behavior. The linear variation makes the device a potential candidate for developing artificial neural networks. PPF underlies how synapses in the human brain achieve STM effects. When two consecutive impulses are applied, the closer the interval between the two excitations, the stronger the excitatory postsynaptic current (EPSC) elicited. As shown in Fig. 4c, a pair of presynaptic optical pulses (359 nm, 1.38 mW/cm^2) was applied to an artificial photo-synaptic device with an illumination time of 100 ms. When the interval was 100 ms, the PPF index was as high as 83.7%. The elevated PPF index indicates that the device can efficiently transmit information to the next stage with minimal signal loss.

Fig. 4d shows the spike-based neuromorphic light interactive behavior based on the FeFETs. After 50 consecutive optical spikes applied to the α-In_2Se_3/MoS_2 device, the optical spike frequency increases from 1.1 Hz to 5 Hz, and the ΔEPSC increases from 0.12 nA to 0.49 nA. After illumination removal, it was followed by sluggish attenuation for more than 100 s; this relaxation process is similar to the LTM effect in the human brain. Besides, we found that the transition from STM to LTM can be achieved by increasing the frequency of the optical spikes. As the pulse frequency increases, the memory effect may last longer. Neuromorphic light interaction behavior depends not only on optical spike frequency but also on duration and intensity. Fig. 4e illustrates the influence of light duration on EPSC increment as well as sluggish attenuation. In the blue (457 nm) and red light (671 nm) wavelength ranges, similar light interaction phenomena can be observed (Fig. S17 in Supporting information). The “Learning-Forgetting-Relearning” model is a necessary pathway for the human brain to achieve LTM, manifested by transitioning from STM to LTM after multiple rehearsals and reinforcements [21]. As shown in Fig. 4f, an optical pulse (359 nm, 1.38 mW/cm^2) with a width of 5 s increases the EPSC from 0.1 nA to 0.26 nA, representing the first learning process. Afterward, a sluggish attenuation process is followed before the next optical pulse arrives, which presents a forgetting process. When experiencing a second learning, the EPSC fully recovers in only 2 s; the relearning process is more accessible, and the information gained is more robust. Demonstration of the “Learning-Forgetting-Relearning” model affirms the feasibility of implementing artificial visual neural networks.

The light adaptation and Pavlovian conditioning of the superior biological visual system are mimicked in Fig. 5. The human eyes have a self-adaptation unconditioned reflex function. When exposed to dazzling optical illumination, they unconsciously adjust the diameter of the iris to reduce the light stimulus it receives, thereby preventing damage to the retina. This reflex phenomenon is commonly known as the "pupil reflex" [16,18]. As depicted in Fig. 5a, the device produces a weak electrical response under regular and weak optical stimuli (30 number, 1.38 mW/cm^2), consistent with the human iris maintaining a constant diameter when exposed to weak visual stimuli. When the device was exposed to dazzling optical stimuli (30 number, 3.45 mW/cm^2), the current level of the device exceeded the threshold (0.4 nA), similar to the iris being unable to work and suffering damage (Fig. 5b). However, when the device was exposed to dazzling optical stimuli while we applied -4.5 V to the gate, the device response current was below the threshold. (Fig. 5c). This phenomenon is highly consistent with the "pupil reflex".

The spatiotemporal correlation behavior of optical and electrical pulses can be utilized to perform classical conditioning reflex experiments on Pavlov’s dog. Fig. 5d illustrates a schematic of the classical conditioning reflex behavior in Pavlov’s dog experiment. When a dog detects food, it automatically salivates, a behavior known as an unconditioned reflex. After training with the bell and food, the dog will also salivate when it hears the bell, which is a conditioned reflex. We mimic the bell ringing process with an optical pulse (1.38 mW/cm^2, 1 s) and the dog’s food detection process with an electrical pulse (5 V, 100 ms). The combination of optical and electrical pulses simulates the training process (Fig. 5e). Repetitive training induces the formation of new synaptic connections in the brain, leading to new associations between adjacent neurons, thus demonstrating the brain’s capacity for event learning. As shown in Fig. 5f, after training, the device current exceeded the threshold applied by optical stimuli, indicating the establishment of an association between the optical and electrical impulses, and that association led to a ‘salivation’ response triggered by optical stimuli.

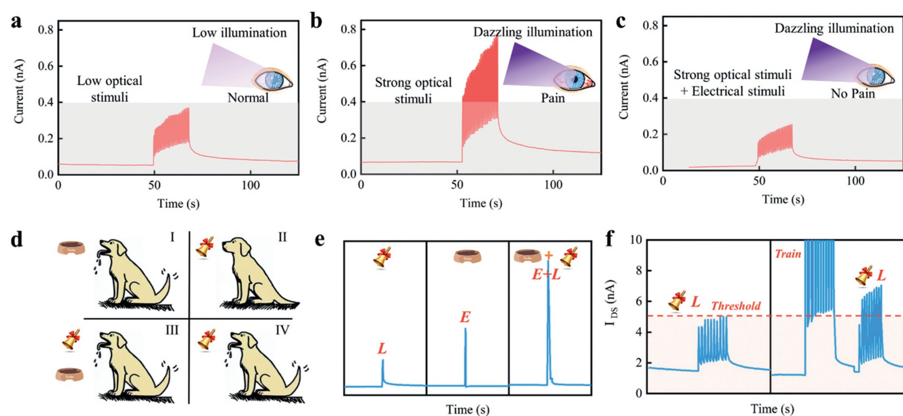

Fig. 5. Simulation superior biological visual system functions. (a) With mild light stimulation, the photocurrent is below the threshold and does not cause any damage to the eyes. (b) With dazzling light stimulation, the photocurrent exceeds the threshold, and the eyes suffer damage. (c) The photo-adaptive behavior of the human eyes suffers dazzling light stimuli. (d) Schematic illustration of Pavlov's dog experiment. Classical Pavlov's dog experiment under (e) one or (f) ten pieces of training.

In summary, we propose a synthetic strategy to grow homogeneous components, large-scale, high crystallinity, and good contact planar/vertical α-In_2Se_3/MoS_2 heterojunctions by dynamically tuning the growth temperature. In addition, we have constructed FeFET devices based on heterostructure that exhibit excellent photoelectricity in the visible wavelengths. On the one hand, this device can achieve multistate storage and logic gate operations through optically assisted polarization switching and electrostatic gating. On the other hand, synergistic modulation of optical and electrical spikes can realize various functions of photo-synapses in biological visual neural systems, such as PPF, STM, LTM, relearning, light adaptation, and Pavlov conditioning. This study provides an approach for synthesizing planar/vertical α-In_2Se_3/MoS_2 heterojunctions and offers unique opportunities to fabricate all-in-one artificial visual neural networks.

Declaration of competing interest

The authors declare that they have no known competing financial interests or personal relationships that could have appeared to influence the work reported in this paper.

Acknowledgments

This work was supported by the National Natural Science Foundation of China (Nos. 52371245, 12174237, 12241403), the National Key Research and Development Program of China (No. 2022YFB3505301).

Supplementary materials

Supplementary material associated with this article can be found, in the online version, at doi:10.1016/j.cclet.2024.109687.

References

[1] S. Seo, J.I. Cho, K.S. Jung, et al., Adv. Mater. 34 (2022) e2202799.
[2] Q. Tao, R. Wu, Q. Li, et al., Nat. Commun. 12 (2021) 1825.
[3] Y. Zhou, L. Tong, Z. Chen, et al., Nat. Commun. 14 (2023) 4270.
[4] P. Singh, D. Rhee, S. Baek, et al., EcoMat 5 (2023) e12333.
[5] M. Hong, X. Zhang, Y. Geng, et al., InfoMat 6 (2024) e12491.
[6] Y. Huang, Y.H. Pan, R. Yang, et al., Nat. Commun. 11 (2020) 2453.
[7] J. Li, X. Yang, Y. Liu, et al., Nature 579 (2020) 368–374.
[8] S. Jia, Z. Jin, J. Zhang, et al., Small 16 (2020) e2002263.
[9] X. Duan, C. Wang, J.C. Shaw, et al., Nat. Nanotechnol. 9 (2014) 1024–1030.
[10] J. You, Z. Jin, Y. Li, et al., Adv. Funct. Mater. (2023) 2311134.
[11] Z. Zou, J. Liang, X. Zhang, et al., ACS Nano 15 (2021) 10039–10047.
[12] X. Wang, B. Zheng, J. Yi, et al., Nano Futures 5 (2021) 015002.
[13] M. Si, P.Y. Liao, G. Qiu, Y. Duan, P.D. Ye, ACS Nano 12 (2018) 6700–6705.
[14] P. Singh, S. Baek, H.H. Yoo, et al., ACS Nano 16 (2022) 5418–5426.
[15] S. Kamaei, X. Liu, A. Saeidi, et al., Nat. Electron. 6 (2023) 658–668.
[16] W. Ci, W. Xue, P. Wang, et al., Adv. Funct. Mater. (2023) 2305822.
[17] P. Wang, J. Li, W. Xue, et al., Adv. Sci. (2023) e2305679.
[18] B. Das, S. Baek, J. Niu, et al., ACS Nano 17 (2023) 21297–21306.
[19] W. Zhang, Q. Su, B. Zhang, J. Peng, Y. Li, ACS Appl. Nano Mater. 6 (2023) 8795–8803.
[20] J. He, R. Wei, S. Ge, et al., InfoMat (2023) e12493.
[21] L. Xu, W. Wang, Y. Li, et al., Nano Res. 10 (2023) 1007.
[22] X. Li, S. Li, J. Tian, et al., Adv. Funct. Mater. (2023) 2306486.
[23] C. Wan, P. Cai, X. Guo, et al., Nat. Commun. 11 (2020) 4602.
[24] Y. Cai, F. Wang, X. Wang, et al., Adv. Funct. Mater. 33 (2022) 2212917.
[25] J. Meng, T. Wang, H. Zhu, et al., Nano Lett. 22 (2022) 81–89.
[26] K. Liu, T. Zhang, B. Dang, et al., Nat. Electron. 5 (2022) 761–773.
[27] F. Xi, A. Grenmyr, J. Zhang, et al., Adv. Electron. Mater. 9 (2022) 2201155.
[28] F. Xue, X. He, D. Periyanagounder, et al., IEEE Trans. Electron. Devices 68 (2021) 1992–1995.
[29] J. Wang, F. Wang, Z. Wang, et al., Sci. Bull. 66 (2021) 2288–2296.
[30] B. Lv, Z. Yan, W. Xue, et al., Mater. Horiz. 8 (2021) 1472–1480.
[31] F. Xue, W. Hu, K.C. Lee, et al., Adv. Funct. Mater. 28 (2018) 1803738.
[32] Y. Hu, H. Yang, J. Huang, et al., ACS Appl. Mater. Interfaces 14 (2022) 55839–55849.
[33] S. Yuan, W.F. Io, J. Mao, et al., ACS Appl. Nano Mater. 3 (2020) 11979–11986.
[34] W.K. Burton, N. Cabrera, F.C. Frank, N.F. Mott, Philos. Trans. R. Soc. London Ser. A 243 (1951) 299–358.
[35] J. Zhou, Q. Zeng, D. Lv, et al., Nano Lett. 15 (2015) 6400–6405.
[36] S. Zhou, L. Liao, J. Chen, et al., ACS Appl. Mater. Interfaces 15 (2023) 23613–23622.
[37] K. Yang, J. Wang, L. Wu, et al., Result. Phys. 51 (2023) 106643.
[38] Q. He, Z. Tang, M. Dai, et al., Nano Lett. 23 (2023) 3098–3105.
[39] Y. Chen, X. Wang, L. Huang, et al., Nat. Commun. 12 (2021) 4030.
[40] G. Wu, X. Zhang, G. Feng, et al., Nat. Mater. 22 (2023) 1499–1506.
[41] B. Zhou, K. Jiang, L. Shang, et al., J. Mater. Chem. C 8 (2020) 11160–11167.
[42] Y.Z. Liu, J.Q. Dai, J. Yuan, M.W. Zhao, Phys. Chem. Chem. Phys. 25 (2023) 33130–33140.
[43] G. Dastgeer, S. Nisar, A. Rasheed, et al., Nano Energy 119 (2024) 109106.